Check for updates

Batteries & Supercaps

Research Article
doi.org/10.1002/batt.202500238

Chemistry Europe
European Chemical Societies Publishing

www.batteries-supercaps.org

Influence of $Al_2(SO_4)_3$ Electrolyte Additive on Cell Potential and Reaction Mechanism in Aqueous Acidic Zn–MnO_2 Batteries

Duk Hyung Jo, Eun Ji Joo, Kwang-Ho Ha, Hyeonbin Kim, Jin Kyu Byun, Sangheon Lee,* and Kyu Tae Lee*

Aqueous Zn–MnO_2 batteries are promising alternatives to lithium-ion batteries due to their inherent safety, low cost, and environmental compatibility. The incorporation of aluminum ions has been shown to enhance their performance by increasing operating voltage and cathode stability. However, the underlying mechanisms remain poorly understood due to complex cathode reactions involving the dissolution, migration, and redeposition of manganese species. Herein, the effects of pH and aluminum sulfate ($Al_2(SO_4)_3$) on the electrochemical performance and reaction mechanisms of Zn–MnO_2 batteries are investigated. The addition of $Al_2(SO_4)_3$ to the electrolyte increases the discharge voltage from 1.4 to ≈1.7 V (vs. Zn/Zn^{2+}), primarily due to changes in the redox potential of the MnO_2 cathode rather than the Zn anode. This enhancement correlates with the maintenance of a highly acidic environment (pH ≈ 1.1), regardless of the presence of Al^{3+}. Additionally, $Al_2(SO_4)_3$ suppresses the formation of zinc hydroxysulfate, typically observed during discharge in $Al_2(SO_4)_3$-free systems, while promoting the precipitation of aluminum hydroxysulfate (AlHS), which is influenced by the depth-of-discharge. The presence of AlHS improves the oxidation kinetics of Mn^{2+} during charging. These findings highlight electrolyte pH and AlHS formation as critical factors in enhancing the electrochemical performance of Zn–MnO_2 batteries.

1. Introduction

The rapid advancement of technology has significantly increased the demand for efficient and reliable energy storage systems (ESSs).[1,2] Lithium-ion batteries (LiBs) have long dominated this sector, serving applications ranging from portable electronic devices to large-scale ESSs, owing to their high energy density and extended cycle life.[3,4] However, their reliance on scarce and costly materials, such as nickel and cobalt, along with safety concerns associated with flammable organic electrolytes,[5–7] has raised questions regarding their long-term sustainability.[8] Among emerging alternative technologies, zinc-ion batteries (ZIBs)[9–13] have garnered considerable interest due to the high theoretical capacity of zinc anodes (820 mA h g^{-1}),[14] cost-effectiveness, environmental compatibility,[15] and inherent safety stemming from their compatibility with aqueous electrolytes.[16–23] Regarding cathode materials, manganese dioxide (MnO_2) stands out as a promising candidate,[24–31] given its natural abundance and high theoretical capacity of 616 mA h g^{-1} achievable via a two-electron redox reaction.[32–36] Despite these notable advantages, the practical implementation of MnO_2 cathodes in ZIBs remains limited by energy density constraints (≈100 Wh kg^{-1})[37–39] primarily due to low cathode utilization, capacity degradation upon prolonged cycling,[25,40–43] and a relatively low redox potential (≈1.4 V vs. Zn/Zn^{2+}).[32,44,45] These factors collectively hinder the further development and commercialization prospects of aqueous Zn–MnO_2 batteries.

To overcome these challenges, various efforts have focused on enhancing the electrochemical performance of Zn–MnO_2 batteries. In particular, the introduction of aluminum ions (Al^{3+}) into aqueous electrolytes[46] has attracted considerable attention due to its reported ability to elevate the operating cell voltage (up to ≈1.7 V vs. Zn/Zn^{2+}),[47–49] improve cathode stability,[50] and mitigate manganese dissolution.[51,52] Li's group proposed a reaction mechanism involving the formation of a Zn-birnessite phase and MnOOH during discharge through Zn^{2+} and H^+ intercalation, and the formation of Al_xMnO_2 phase during charging.[47] Balland's group suggested that Al^{3+} predominantly acts as a proton donor via the $[Al(H_2O)_6]^{3+}$ complex, thereby facilitating more efficient MnO_2 redox reactions and enabling a two-electron transfer process.[51] Nevertheless, the electrochemical reaction mechanisms resulting from the addition of Al^{3+} remain incompletely understood. One of the primary challenges in clarifying the precise role of Al^{3+} lies in the complex reaction environment inherent to Zn–MnO_2 batteries. Unlike LiBs, in which lithium ions move within a stable intercalation framework, the Zn–MnO_2 system involves dissolution, migration, and

D. H. Jo, E. J. Joo, K.-H. Ha, H. Kim, J. K. Byun, K. T. Lee
School of Chemical and Biological Engineering
Institute of Chemical Processes
Institute of Engineering Research
Seoul National University
1-Gwanak-ro, Gwanak-gu, Seoul 08826, Republic of Korea
E-mail: ktlee@snu.ac.kr

S. Lee
Department of Chemical Engineering and Materials Science
Ewha Womans University
52, Ewhayeodae-gil, Seodaemun-gu, Seoul 03760, Republic of Korea
E-mail: sang@ewha.ac.kr

Supporting information for this article is available on the WWW under https://doi.org/10.1002/batt.202500238

© 2025 Wiley-VCH GmbH

Research Article
doi.org/10.1002/batt.202500238
Chemistry Europe
European Chemical Societies Publishing

redeposition of manganese species,[32,53] complicating the isolation and detailed study of individual reaction pathways.

In this work, we elucidated the reaction mechanisms underlying the enhanced operating cell voltage observed in Zn–MnO_2 batteries with $Al_2(SO_4)_3$ electrolyte additives by employing comprehensive electrochemical, structural, and spectroscopic analyses of both the MnO_2 cathode and the electrolyte components. Our study also provides evidence for the formation of aluminum hydroxysulfate species during discharge, which play a role in determining the kinetics of Mn^{2+} oxidation into manganese oxides.

2. Results and Discussion

2.1. Role of pH in Increasing Cell Potential of Zn-MnO_2 Batteries Containing $Al_2(SO_4)_3$ Electrolyte Additives

Zn–MnO_2 batteries, both with and without $Al_2(SO_4)_3$ electrolyte additives, were assembled into coin cells using α-MnO_2 cathodes and zinc metal foil anodes to investigate the reaction mechanism influenced by $Al_2(SO_4)_3$. The α-MnO_2 nanorods were synthesized via a hydrothermal method.[54,55] A baseline aqueous electrolyte containing 2 M $ZnSO_4$ (without Al^{3+}) was compared against a variable electrolyte containing 1 M $ZnSO_4$ and 0.5 M $Al_2(SO_4)_3$, with both electrolytes having equal cation concentrations. **Figure 1**a,b illustrates the voltage profiles for the first two cycles of Zn–MnO_2 batteries without and with $Al_2(SO_4)_3$, respectively. The cells containing the Al^{3+} additive exhibited higher redox potentials than cells without the additive, showing discharge plateaus at ≈1.7 V (vs. Zn/Zn^{2+}) compared to ≈1.4 V (vs. Zn/Zn^{2+}) in the baseline electrolyte. Galvanostatic intermittent titration technique (GITT) profiles further supported these observations, displaying higher quasi-open-circuit voltages (QOCVs) in the electrolyte with the Al^{3+} additive (Figure 1c). However, the reduced Coulombic efficiency observed in the electrolyte containing Al^{3+} was attributed to the competitive oxygen evolution reaction occurring simultaneously at potentials above 1.23 V (vs. standard hydrogen electrode). To differentiate the contributions of the cathode and anode to the increased redox potential, a three-electrode H-cell configuration was assembled, as shown in Figure 1d. The MnO_2 cathode and Zn anode were placed in separate chambers, divided by a Nafion-117 membrane to prevent Al^{3+} ion crossover. The anode chamber contained 2 M $ZnSO_4$, while the cathode chamber contained 1 M $ZnSO_4$ and 0.5 M $Al_2(SO_4)_3$. An Ag/AgCl reference electrode was employed for precise cathode potential measurements. The voltage profile of the three-electrode H-cell closely mirrored that of the coin cell with Al^{3+} additive, achieving a higher discharge capacity of ≈500 mA h g^{-1} (Figure 1e). These results imply that the increased cell voltage observed with the Al^{3+} additive originates from the MnO_2 cathode (Figure 1f). This is attributed to the consistent Zn anode reactions across both electrolytes, suggesting unchanged anode potentials, as the Zn anode side employed the same 2 M $ZnSO_4$ electrolyte. However, the poor charge capacity of the H-cell compared to the coin cell was attributed to the large electrolyte volume and the increased distance between electrodes. These modifications in cell configuration promote the diffusion of dissolved manganese ions into the bulk electrolyte, thereby, hindering their redeposition during charging due to mass transport limitations.

To demonstrate the increase in cell potential of Zn–MnO_2 batteries with $Al_2(SO_4)_3$ electrolyte additives compared to those without $Al_2(SO_4)_3$, we compared the voltage profiles of Zn–MnO_2 cells at various electrolyte pH levels, as shown in **Figure 2**a. The

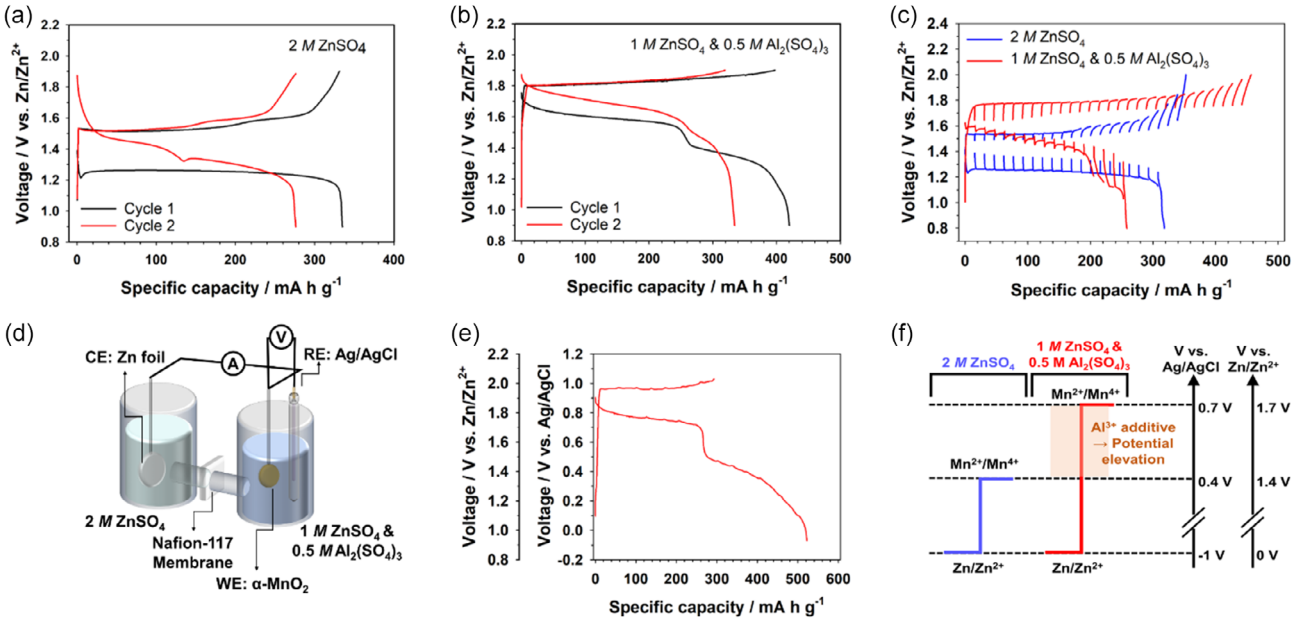

Figure 1. Voltage profiles of Zn–MnO_2 cells with a) 2 M $ZnSO_4$ (without Al^{3+} additive) and b) 1 M $ZnSO_4$ and 0.5 M $Al_2(SO_4)_3$, at a specific rate of 0.3C (92.5 mA g^{-1}) for the first (black) and second (red) cycles. c) GITT profiles of Zn–MnO_2 cells with i) 2 M $ZnSO_4$ (blue) and ii) 1 M $ZnSO_4$ and 0.5 M $Al_2(SO_4)_3$ (red). d) A three-electrode H-cell configuration (MnO_2 | $ZnSO_4$, $Al_2(SO_4)_3$ || $ZnSO_4$ | Zn) and e) corresponding voltage profiles. f) Schematic illustration showing the enhancement of cell potential facilitated by the MnO_2 side upon adding Al^{3+} additive.

© 2025 Wiley-VCH GmbH

25666223, 0, Downloaded from https://chemistry-europe.onlinelibrary.wiley.com/doi/10.1002/batt.202500238 by University of Ulsan, Wiley Online Library on [11/11/2025]. See the Terms and Conditions (https://onlinelibrary.wiley.com/terms-and-conditions) on Wiley Online Library for rules of use; OA articles are governed by the applicable Creative Commons License

Research Article
doi.org/10.1002/batt.202500238
Chemistry Europe
European Chemical Societies Publishing

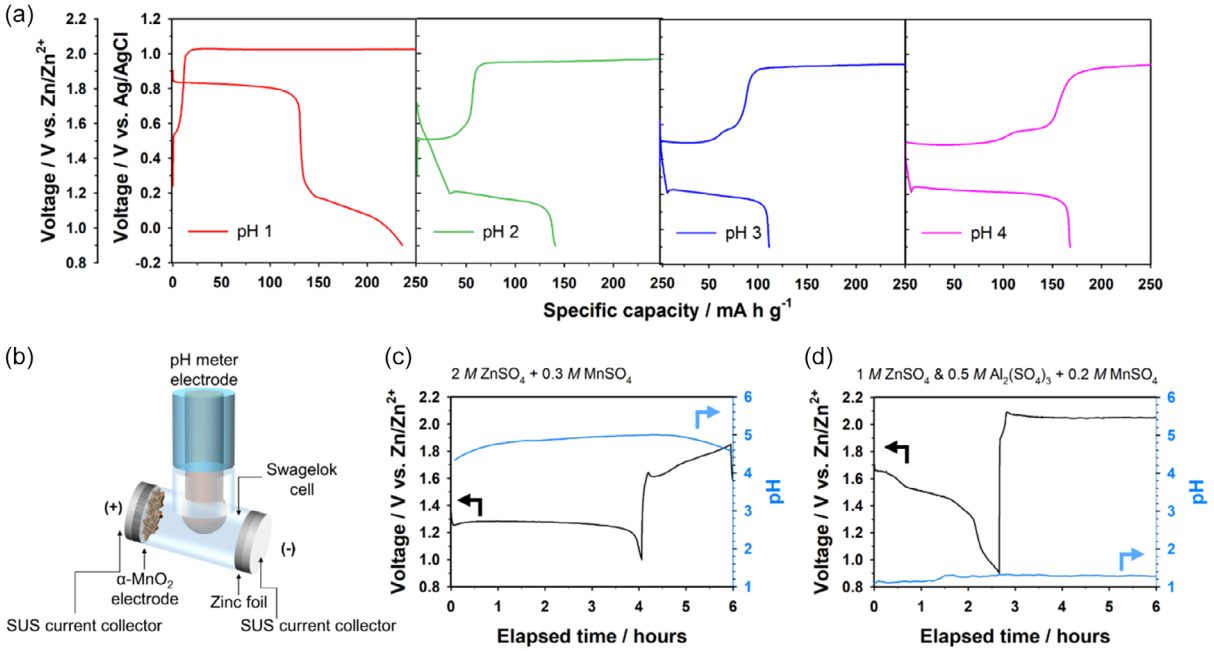

Figure 2. a) Voltage profiles for Zn–MnO_2 cells with 1 M $ZnSO_4 + 0.2$ M $MnSO_4$ (without Al^{3+} additives) at various pH levels. The current density was 0.3C (92.5 mA g^{-1}). b) Schematic of the electrochemical cell designed for operando pH analysis. c,d) Voltage profiles and corresponding pH variations in Zn–MnO_2 cells (c) without and d) with Al^{3+} additives.

pH of the electrolytes was adjusted by adding H_2SO_4. When the pH of the bare electrolyte (1 M $ZnSO_4 + 0.2$ M $MnSO_4$) was between 2 and 4, the voltage profiles closely resembled those of typical mild-acid Zn–MnO_2 batteries. However, at pH = 1, the voltage profiles of Zn–MnO_2 cells without $Al_2(SO_4)_3$ were almost identical to those with $Al_2(SO_4)_3$. Additionally, we investigated pH changes in the electrolyte during charge and discharge in MnO_2 | $ZnSO_4$, $Al_2(SO_4)_3$ | Zn metal cells using operando pH analysis. Figure 2b shows a schematic of the cell configuration used for this analysis, where the pH meter was placed between the MnO_2 and Zn electrodes. Real-time pH measurements were taken during cycling within a voltage range of 1.0–2.0 V (vs. Zn/Zn^{2+}) for two electrolytes: 2 M $ZnSO_4$ and a mixture of 1 M $ZnSO_4$ and 0.5 M $Al_2(SO_4)_3$ (Figure 2c,d, respectively). In the 2 M $ZnSO_4$ electrolyte without $Al_2(SO_4)_3$, the pH of the electrolyte varied between 4 and 5 during cycling. Specifically, the pH gradually increased during initial discharge. This is attributed to the oxidation of MnO_2 to Mn^{2+}, which consumes H^+ ions and releases OH^-, accompanied by the formation of zinc hydroxysulfate (ZHS).[56,57] During the subsequent charge, the pH decreased reversibly as OH^- ions released due to ZHS dissolution were consumed to form manganese oxides and release H^+ ions.[58] In contrast, for the 1 M $ZnSO_4$ and 0.5 M $Al_2(SO_4)_3$ electrolyte, the pH remained nearly constant at ≈1.1 throughout charge and discharge, owing to the highly acidic nature of $Al_2(SO_4)_3$. This acidity originates from the hydrolysis of water promoted by the strong Lewis acidity of Al^{3+} ions.[59] This reveals that the higher cell potential observed in Zn–MnO_2 batteries with $Al_2(SO_4)_3$ electrolyte additives is attributed to the reversible redox behavior of MnO_2 in the highly acidic environment (pH ≈ 1.1).

To isolate the effect of pH from that of anionic species, two acids—sulfuric acid and hydrochloric acid—were employed to adjust the electrolyte pH to 1, thereby introducing distinct anionic environments. **Figure 3**a,b compares the voltage profiles of Zn–MnO_2 cells cycled in 2 M $ZnSO_4 + 0.2$ M $MnSO_4$ electrolytes, acidified to pH 1 using H_2SO_4 and HCl, respectively. Despite the different anions introduced, both electrolytes exhibited nearly identical voltage profiles, with discharge plateaus at ≈0.9 V (vs. Ag/AgCl), corresponding to ≈1.9 V (vs. Zn/Zn^{2+}). Furthermore, Figure 3c shows the voltage profile of Zn–MnO_2 cells with 1 M $ZnSO4 + 0.5$ M $Al_2(SO_4)_3 + 0.2$ M $MnSO_4$, also adjusted to pH 1 with H_2SO_4. The voltage profile remained consistent regardless of the presence of Al^{3+}. This reveals that the elevated redox potential of Zn–MnO_2 cells is governed primarily by electrolyte pH rather than the salt species of additives.

2.2. Formation of Aluminum Hydroxysulfates during Discharge

To elucidate the reaction mechanism of Zn–MnO_2 cells with Al^{3+} additives, structural changes in the MnO_2 cathode were examined during the initial cycle. We performed ex situ X-ray diffraction (XRD) and X-ray absorption near-edge structure (XANES) analyses at various depth-of-discharge (DOD) and state-of-charge (SOC) levels, as shown in **Figure 4**a. The XRD patterns of the MnO_2 cathode at different stages are shown in Figure 4b. The (110) peak intensity of α-MnO_2 at 12° gradually decreased from point (i) to point (viii) during discharge, without the appearance of new peaks or any noticeable peak shift. This suggests that the reduced form of MnO_2 during discharge was either amorphous or dissolved in the electrolyte. Remarkably, no zinc hydroxysulfate

© 2025 Wiley-VCH GmbH

25666223, 0, Downloaded from https://chemistry-europe.onlinelibrary.wiley.com/doi/10.1002/batt.202500238 by University of Ulsan, Wiley Online Library on [11/11/2025]. See the Terms and Conditions (https://onlinelibrary.wiley.com/terms-and-conditions) on Wiley Online Library for rules of use; OA articles are governed by the applicable Creative Commons License

Research Article
doi.org/10.1002/batt.202500238
Chemistry Europe
European Chemical Societies Publishing

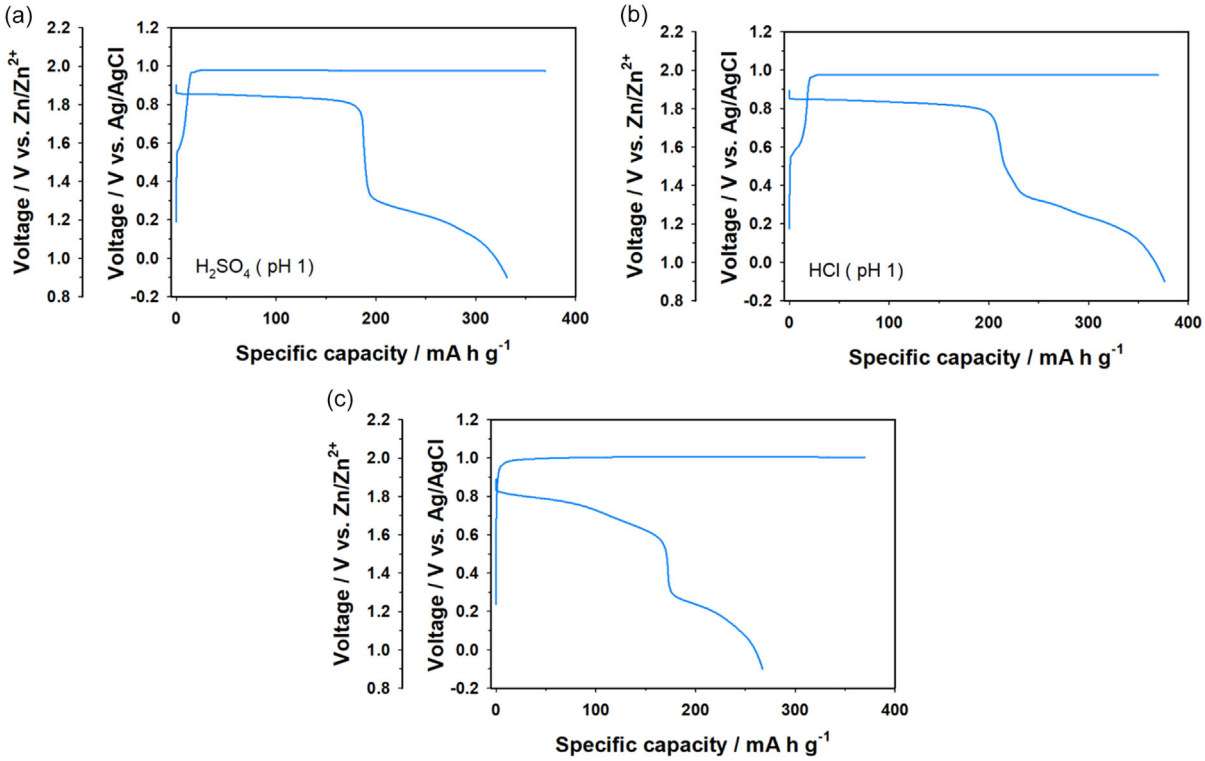

Figure 3. Voltage profiles of Zn–MnO_2 cells cycled in 2 M $ZnSO_4$ + 0.2 M $MnSO_4$ electrolytes, adjusted to pH = 1 using a) H_2SO_4 and b) HCl. c) Voltage profile of Zn–MnO_2 cells cycled in 2 M $ZnSO_4$ and 0.5 M $Al_2(SO_4)_3$ + 0.2 M $MnSO_4$, adjusted to pH = 1 using H_2SO_4.

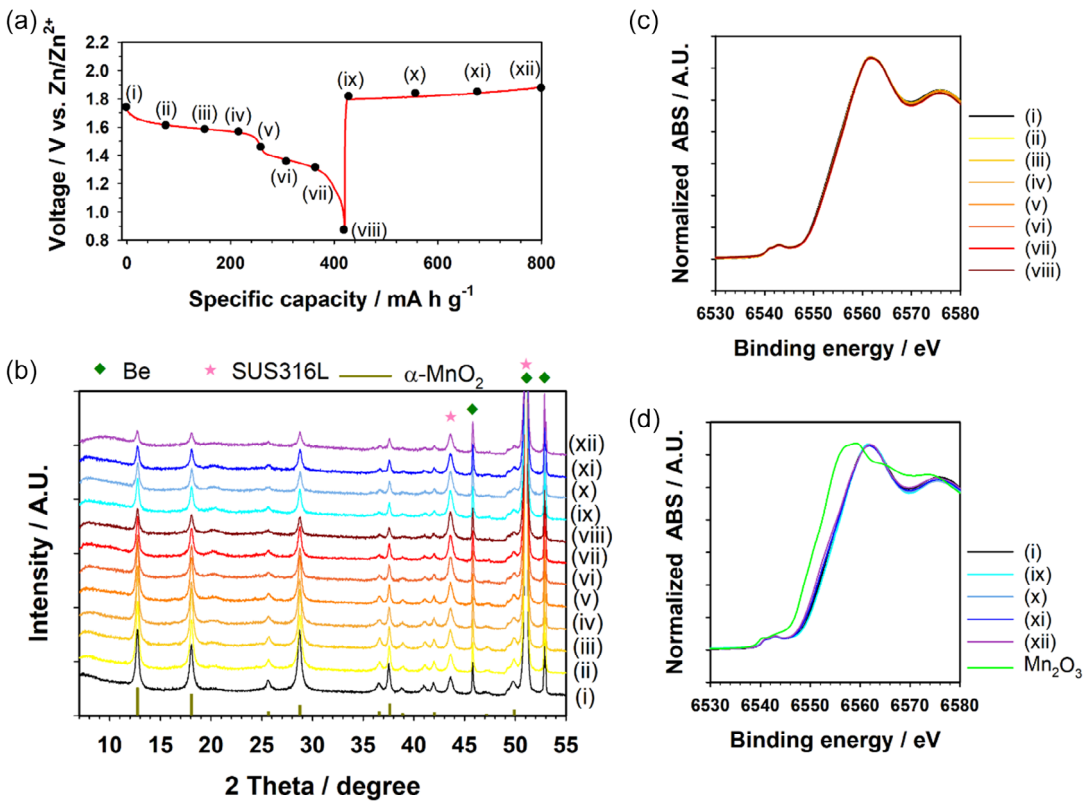

Figure 4. a) Voltage profile of Zn–MnO_2 cells with 1 M $ZnSO_4$ and 0.5 M $Al_2(SO_4)_3$ for the initial cycle. b) Ex situ XRD patterns of the α-MnO_2 cathodes retrieved at various discharge/charge states indicated in the voltage profile of (a). c,d) Ex situ Mn K edge XANES spectra of the α-MnO_2 cathodes retrieved at various (c) discharge and (d) charge states indicated in the voltage profile of (a).

© 2025 Wiley-VCH GmbH

25666223, 0, Downloaded from https://chemistry-europe.onlinelibrary.wiley.com/doi/10.1002/batt.202500238 by University of Ulsan, Wiley Online Library on [11/11/2025]. See the Terms and Conditions (https://onlinelibrary.wiley.com/terms-and-conditions) on Wiley Online Library for rules of use; OA articles are governed by the applicable Creative Commons License

Research Article
doi.org/10.1002/batt.202500238
Chemistry Europe
European Chemical Societies Publishing

(ZHS) phase—typically observed around 10°—appeared during discharge, whereas ZHS peaks were clearly detected in the baseline electrolyte without Al^{3+} (Figure S1, Supporting Information). This indicates that the $Al_2(SO_4)_3$ additive suppressed the formation of ZHS during discharge. Figure 4c,d presents the XANES spectra of the MnO_2 cathodes during discharge and subsequent charge, respectively. The XANES spectra remained nearly unchanged during discharge with negligible shifts in the Mn absorption edge, suggesting that manganese largely retained its Mn^{4+} oxidation state throughout discharge. These results suggest the fact that the reduced species of MnO_2 were dissolved into the electrolyte rather than undergoing a structural transformation into amorphous phases, consistent with the ex situ XRD observations. However, during subsequent charging, a slight but progressive shift toward lower energy values in the XANES spectra was observed. This implies a gradual decrease in the oxidation state of manganese, despite the expectation of oxidation during charge. Compared to Mn_2O_3 (Mn^{3+}) as a reference, the edge shift does not fully align with Mn(III), remaining closer to Mn(IV). This suggests the deposition of Mn-containing oxides with an intermediate oxidation state between Mn^{3+} and Mn^{4+}. These findings indicate that Mn^{2+} ions dissolved in the electrolyte were oxidized and precipitated in the form of A_xMnO_2 (A = Mn, Zn, Al, or their combinations).

The dissolution and precipitation of MnO_2 during discharge and charge, respectively, were confirmed by ex situ inductively coupled plasma atomic emission spectroscopy (ICP-AES) and electron paramagnetic resonance (EPR) analyses. We performed ex situ ICP-AES to quantify the amount of manganese species remaining in the liquid electrolytes and solid electrodes retrieved at various DOD and SOC levels, as shown in **Figure 5**a. The Mn concentrations in the MnO_2 cathode and the electrolyte at different states are presented in Figure 5b. The Mn concentration in the cathode gradually decreased during discharge and subsequently increased during charging. Correspondingly, the Mn concentration in the electrolyte increased during discharge and decreased during charge. This indicates that MnO_2 dissolved into Mn^{2+} ions in the electrolyte during discharge, and that Mn^{2+} was oxidized and precipitated as manganese oxides during charge. This fact is further supported by the ex situ EPR analysis shown in Figure 5c. A characteristic sextet hyperfine pattern indicative of Mn^{2+} ions appeared after discharge, whereas a notable decrease in the intensity of the EPR signal of Mn^{2+} was observed after charge.

To further clarify the reaction mechanism of Zn–MnO_2 cells with Al^{3+} additives, changes in the MnO_2 cathode during the initial cycle were investigated using ex situ scanning electron microscopy with energy-dispersive spectroscopy (SEM/EDS), ICP-AES, and X-ray photoelectron spectroscopy (XPS). **Figure 6**a,b shows the SEM/EDS mapping images and the corresponding EDS spectrum of the MnO_2 cathode retrieved after full discharge. Aluminum and sulfur elements were clearly detected on the MnO_2 cathode surface, suggesting that Al^{3+} from the electrolyte precipitated during discharge. This observation is further supported by ex situ ICP-AES analysis (Figure 6c), which shows a decrease in the Al concentration in the electrolyte and a corresponding increase in the MnO_2 cathode after discharge. Figure S2, Supporting Information, presents the Fourier transform infrared (FT-IR) spectrum and

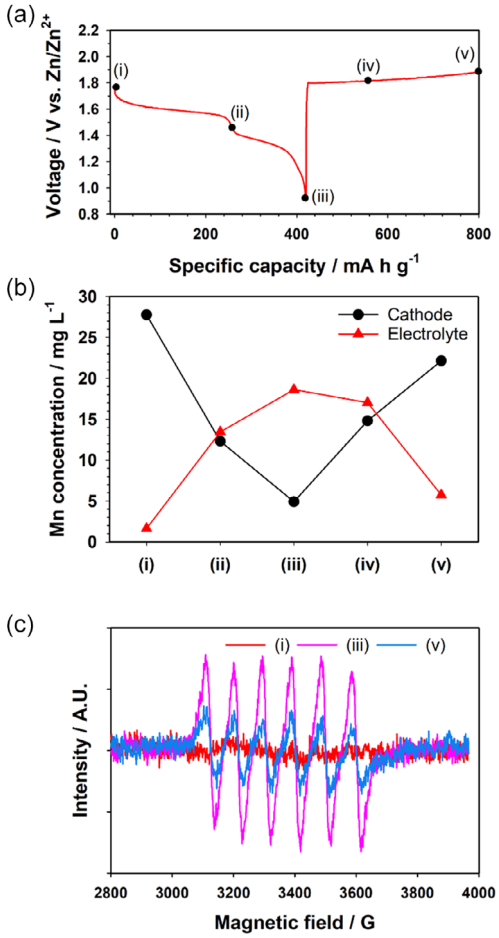

Figure 5. a) Voltage profile of Zn–MnO_2 cells with 1 M $ZnSO_4$ and 0.5 M $Al_2(SO_4)_3$ for the initial cycle. b) Mn concentrations in the MnO_2 cathode and the electrolyte of Zn–MnO_2 cells retrieved at various discharge/charge states indicated in the voltage profile of (a). c) Ex situ EPR spectra of the electrolytes retrieved at various discharge/charge states indicated in the voltage profile of (a).

XRD pattern of aluminum hydroxysulfate ($Al_4(SO_4)(OH)_{10}{\cdot}5H_2O$, denoted as AlHS) powders synthesized via conventional acid–base precipitation.[60] Characteristic peaks corresponding to hydroxyl and sulfate functional groups—at 555, 1001, 1092, 1636, and 3376 cm^{-1}, assigned to Al—O, Al—OH, SO_4^{2-}, $(H_2O){\cdot}OH^{-1}$, and OH^- vibrations, respectively[61–63]—were observed in the FT-IR spectrum of AlHS powders. The XRD pattern also indicates that the AlHS powders are poorly crystalline. Figure S3, Supporting Information, shows the SEM/EDS mapping images and EDS spectrum of the synthesized AlHS, which are nearly identical to those of the MnO_2 cathode retrieved after full discharge. This implies that Al^{3+} in the electrolyte precipitated in the form of AlHS during discharge. A key difference in the reaction mechanisms of Zn–MnO_2 batteries with and without $Al_2(SO_4)_3$ electrolyte additives lies in the formation of AlHS and ZHS, respectively, during discharge. In Zn–MnO_2 batteries without $Al_2(SO_4)_3$, ZHS formed during discharge, rather than manganese hydroxy sulfates (denoted as MnHS). In contrast, in cells with $Al_2(SO_4)_3$, only AlHS formed during discharge, whereas ZHS and MnHS did not form. This difference is attributed to the different solubility products (K_{SP}) of MnHS, ZHS,

© 2025 Wiley-VCH GmbH

25666223, 0, Downloaded from https://chemistry-europe.onlinelibrary.wiley.com/doi/10.1002/batt.202500238 by University of Ulsan, Wiley Online Library on [11/11/2025]. See the Terms and Conditions (https://onlinelibrary.wiley.com/terms-and-conditions) on Wiley Online Library for rules of use; OA articles are governed by the applicable Creative Commons License

Research Article
doi.org/10.1002/batt.202500238
Chemistry Europe
European Chemical Societies Publishing

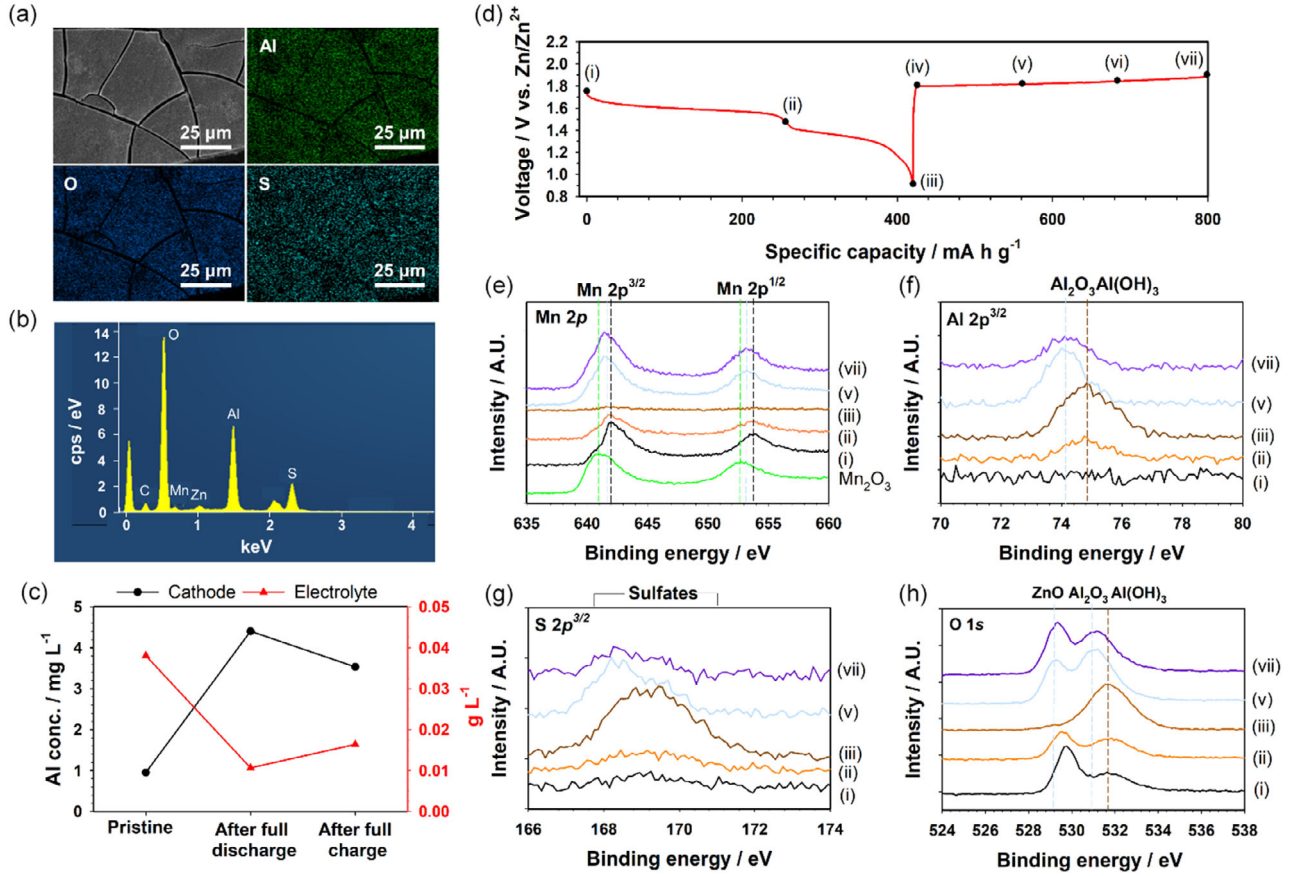

Figure 6. a) Ex situ SEM and EDS mapping images and b) the corresponding EDS spectrum of the MnO_2 cathode retrieved after full discharge. c) Al concentrations in the MnO_2 cathode and the electrolyte of Zn–MnO_2 cells retrieved at various discharge/charge states. d) Voltage profile of Zn–MnO_2 cells with 1 M $ZnSO_4$ and 0.5 M $Al_2(SO_4)_3$ for the initial cycle. Ex situ e) Mn 2p, f) Al 2p, g) S 2p, and h) O 1s XPS spectra of the α-MnO_2 cathodes retrieved at various discharge/charge states indicated in the voltage profile of (d).

and AlHS in aqueous solutions. The K_{SP} values for $Mn(OH)_2$, $Zn(OH)_2$, and $Al(OH)_3$ are presented in Table S1, Supporting Information.[64]

In addition, we performed ex situ XPS analysis on the MnO_2 cathodes retrieved at various DOD and SOC levels, as shown in Figure 6d. Figure 6e–h shows the Mn 2p, Al 2p, S 2p, and O 1s XPS spectra of the MnO_2 cathodes, respectively. At point (i), the Mn 2p XPS spectra exhibited prominent peaks at 643 eV ($2p^{3/2}$) and 654 eV ($2p^{1/2}$), with a spin-orbit splitting of 11 eV, characteristic of Mn^{4+} in α-MnO_2. Negligible Al 2p and S 2p signals revealed the absence of aluminum and sulfate species on the electrode surface. During discharge at the first plateau (≈1.6 V vs. Zn/Zn^{2+}), the intensity of the Mn 2p peaks decreased, indicating partial dissolution of MnO_2 to Mn^{2+} ions to the electrolyte. This was further supported by the O 1s spectra, which retained a Mn—O bond signal at 530.2 eV and showed an emerging hydroxyl-related peak at 531.8 eV, suggesting localized hydrolysis during MnO_2 reduction. Al 2p and S 2p signals remained negligible at this stage. After full discharge, Mn 2p peaks vanished entirely, even if MnO_2 was not completely dissolved. Given the surface sensitivity of XPS, this suggests that the MnO_2 surface was fully covered by AlHS. This interpretation is corroborated by the appearance of a hydroxide-related Al 2p peak at 74.5 eV, a sulfate-related S 2p peak at 169.1 eV, and a new O 1s peak assigned to $Al(OH)_3$. These observations indicate that AlHS formation was absent at the first plateau (≈1.6 V vs. Zn/Zn^{2+}) of the voltage profile and occurred primarily during the second plateau (≈1.4 V vs. Zn/Zn^{2+}), as detailed below.

At the first plateau (≈1.6 V vs. Zn/Zn^{2+})

$$MnO_2(s) + Zn(s) + 2H^+(aq) \rightarrow Mn^{2+}(aq) + 2OH^-(aq) + Zn^{2+}(aq) \quad (1)$$

At the second plateau (≈1.4 V vs. Zn/Zn^{2+})

$$5MnO_2(s) + 5Zn(s) + 4Al^{3+}(aq) + 10H^+(aq) + SO_4^{2-}(aq) + 5H_2O(l) \rightarrow 5Mn^{2+}(aq) + Al_4(SO_4)(OH)_{10} \cdot 5H_2O(s) + 5Zn^{2+}(aq) \quad (2)$$

As shown in Figure 1c, the overpotential of the second discharge plateau at ≈1.4 V (vs. Zn/Zn^{2+}) was notably higher than that of the first at ≈1.6 V (vs. Zn/Zn^{2+}). This suggests that the increased overpotential at the second discharge plateau is correlated with the formation of AlHS during discharge. During the subsequent charge, the Mn 2p signal reemerged at a slightly lower binding energy (641.8 eV), indicating the reprecipitation of manganese oxides with an average oxidation state lower than +4. This observation aligns with the ex situ XANES results shown

© 2025 Wiley-VCH GmbH

25666223, 0, Downloaded from https://chemistry-europe.onlinelibrary.wiley.com/doi/10.1002/batt.202500238 by University of Ulsan, Wiley Online Library on [11/11/2025]. See the Terms and Conditions (https://onlinelibrary.wiley.com/terms-and-conditions) on Wiley Online Library for rules of use; OA articles are governed by the applicable Creative Commons License

in Figure 4d. The shift is attributed to the formation of Zn- and Al-substituted manganese oxides, consistent with previous reports.[47] Concurrently, the Al 2p peak shifted to a lower binding energy, suggesting the formation of aluminum oxides, while the S 2p signal diminished, indicating the release of sulfate species back into the electrolyte. These changes imply that AlHS was progressively decomposed and formed Zn- and Al-inserted manganese oxides during charge. This interpretation is further supported by ex situ ICP-AES analysis, which shows that Al concentrations in both the electrolyte and the MnO_2 cathode changed slightly during charge, while changing significantly during the preceding discharge (Figure 6c). This provides additional evidence that Al^{3+} in AlHS was transformed into Zn- and Al-inserted manganese oxides during the charging process.

The formation of AlHS during the second discharge plateau (≈1.4 V vs. Zn/Zn^{2+}) is also supported by the observed changes in charge overpotential for two different voltage ranges. **Figure 7**a presents the voltage profiles of MnO_2 | $ZnSO_4$, $Al_2(SO_4)_3$ | Zn cells over two distinct voltage ranges: i) 1.4–1.9 V and ii) 0.9–1.9 V. When the cell was discharged to the lower voltage of 0.9 V, compared to 1.4 V, the charge overpotential was noticeably reduced. This behavior is more evident in the dQ/dV plots of the charge profiles for both voltage ranges, as shown in Figure 7b. In the voltage range of 1.4–1.9 V (vs. Zn/Zn^{2+}), the formation of AlHS was negligible. Therefore, the oxidation of Mn^{2+} to $Zn_xAl_yMnO_2$ during charge primarily proceeds via water decomposition, as described by Equation (3). This reaction is known to be kinetically sluggish, resulting in large overpotential,

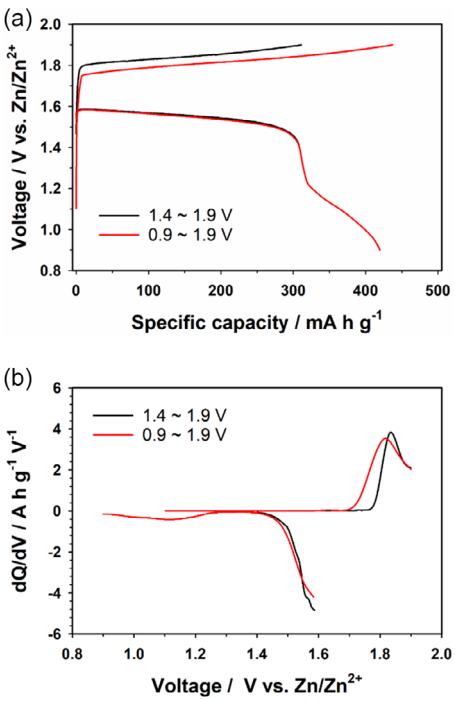

Figure 7. a) Voltage profile of Zn–MnO_2 cells with 1 M $ZnSO_4$ and 0.5 M $Al_2(SO_4)_3$ in two distinct voltage ranges: i) 1.4–1.9 V (black) and ii) 0.9–1.9 V (red) and b) corresponding dQ/dV plots. The current density was 0.3C (92.5 mA g^{-1}).

as demonstrated in our previous literature.[58] However, in conventional mild-acid Zn–MnO_2 batteries without Al^{3+}, ZHS, including $Zn_4(OH)_6SO_4$, forms during discharge and then decomposes during charge, releasing OH^-. This OH^- is known to facilitate the oxidation of Mn^{2+} to MnO_2, thereby reducing the overpotential compared to the water decomposition route in Equation (3).[58] Similarly, when the cell is discharged to 0.9 V (in the 0.9–1.9 V range), the oxidation of Mn^{2+} to $Zn_xAl_yMnO_2$ during charging is accompanied by the decomposition of AlHS. The role of AlHS is analogous to the role of ZHS in conventional Zn–MnO_2 systems without Al^{3+} additives. As a result, the charge overpotential in the 0.9–1.9 V range (vs. Zn/Zn^{2+}) was lower than that in the 1.4–1.9 V range.

Voltage range of 1.4−1.9 V (vs. Zn/Zn^{2+})

$$Mn^{2+}(aq) + 2H_2O(l) + xZn^{2+}(aq) + yAl^{3+}(aq) \rightarrow Zn_xAl_yMnO_2(s) + 4H^+(aq) + 2e^- \quad (3)$$

Voltage range of 0.9−1.9 V (vs. Zn/Zn^{2+})

$$5Mn^{2+}(aq) + Al_4(SO_4)(OH)_{10} \cdot 5H_2O(s) + 5xZn^{2+}(aq) \rightarrow 5Zn_xAl_yMnO_2(s) + 10H^+(aq) + (4-5y)Al^{3+}(aq) + SO_4^{2-} - (aq) + 5H_2O(l) + ze^- \quad (4)$$

3. Conclusion

We investigated the influence of pH and aluminum sulfate ($Al_2(SO_4)_3$) on the cell potential and reaction mechanisms of Zn–MnO_2 batteries. The introduction of $Al_2(SO_4)_3$ into the electrolyte significantly increased the discharge potential, resulting in a higher voltage plateau of ≈1.7 V (vs. Zn/Zn^{2+}), compared to 1.4 V (vs. Zn/Zn^{2+}) in the pristine $ZnSO_4$ electrolyte. A three-electrode H-cell setup was employed to separately examine the anode and cathode behaviors, revealing that the MnO_2 cathode primarily accounts for the voltage enhancement. The cell potential was found to be highly dependent on electrolyte pH, reaching ≈1.8 V (vs. Zn/Zn^{2+}) at pH = 1, despite the absence of $Al_2(SO_4)_3$. The addition of $Al_2(SO_4)_3$ maintained a strongly acidic environment (pH ≈ 1.1) during both charge and discharge, thereby contributing to the elevated cell potential.

We further explored the role of $Al_2(SO_4)_3$ in the reaction mechanisms of Zn–MnO_2 cells using various ex situ analyses, including XRD, XANES, XPS, EPR, and ICP-AES. Notably, the formation of zinc hydroxysulfate (ZHS), typically observed during discharge in $Al_2(SO_4)_3$-free systems, was suppressed. Instead, aluminum hydroxysulfate (AlHS) precipitated on the MnO_2 cathode surface. This shift is attributed to the lower solubility product of AlHS relative to ZHS. The AlHS precipitation was found to depend on the DOD levels. During charge, the presence of AlHS on the cathode significantly enhanced the oxidation kinetics of Mn^{2+} back to manganese oxides. Therefore, both electrolyte pH and the precipitation behavior of AlHS are key factors in improving the electrochemical performance of Zn–MnO_2 batteries.

© 2025 Wiley-VCH GmbH

25666223, 0, Downloaded from https://chemistry-europe.onlinelibrary.wiley.com/doi/10.1002/batt.202500238 by University of Ulsan, Wiley Online Library on [11/11/2025]. See the Terms and Conditions (https://onlinelibrary.wiley.com/terms-and-conditions) on Wiley Online Library for rules of use; OA articles are governed by the applicable Creative Commons License

25666223, 0, Downloaded from https://chemistry-europe.onlinelibrary.wiley.com/doi/10.1002/batt.202500238 by University of Ulsan, Wiley Online Library on [11/11/2025]. See the Terms and Conditions (https://onlinelibrary.wiley.com/terms-and-conditions) on Wiley Online Library for rules of use; OA articles are governed by the applicable Creative Commons License

4. Experimental Section

Material Synthesis

α-MnO_2 nanorods were synthesized via a hydrothermal method. Specifically, 3.75 g of $KMnO_4$ (99%, Sigma-Aldrich) and 0.21 g of $MnSO_4{\cdot}H_2O$ (99%, Sigma-Aldrich) were dissolved in 240 mL of deionized (DI) water in a 300 mL Teflon-lined autoclave. The mixture was stirred for 10 min and then heated at 180 °C for 14 h. The resulting product was filtered, thoroughly washed with DI water, and dried at 80 °C for 12 h. Aluminum hydroxysulfate (AlHS) powders were prepared by titrating 30 mL of 0.05 mol kg^{-1} $Al_2(SO_4)_3{\cdot}18H_2O$ (97%, Sigma-Aldrich) with 214 mL of 0.015 mol kg^{-1} $Ca(OH)_2$ solution, added dropwise. The resulting powder was then filtered, washed with DI water and ethanol, and dried at 60 °C for 4 h.

Material Characterization

XRD patterns of the powders and electrodes were collected using a Bruker D2 PHASER with Cu Kα radiation ($\lambda = 1.5418$ Å), operated over a 2θ range of 7°–80°, with an airtight sample holder containing a Be window used as an internal reference. The structural properties of the synthesized AlHS were analyzed using FT-IR with a Bruker TENSOR27 instrument in attenuated total reflection mode. Surface morphology and elemental mapping of the electrodes and synthesized AlHS were examined using field emission scanning electron microscopy (FE-SEM, Zeiss, GeminiSEM 560 & SUPRA 55VP) at an accelerating voltage of 5 kV. X-ray absorption spectroscopy of discharged and charged cathodes was conducted in transmission mode at the 8C (Nano XAFS) beamline of the Pohang light source-II, located at the Pohang Accelerator Laboratory (PAL), Korea. X-Ray photoelectron spectroscopy (XPS, Kratos Axis Supra+) was performed to analyze the surface composition of the cathodes. The concentrations of Mn^{2+} and Al^{3+} ions dissolved in the electrolyte and cathode were quantified using inductively coupled plasma atomic emission spectroscopy (ICP-AES, PerkinElmer Optima 8300). EPR spectra of the electrolyte retrieved at various charge and discharge states were recorded using a Bruker EMXmicro-9.5/2.7 X-band spectrometer with an E4119001 cavity, operating at X-band frequencies (9.4 GHz). The magnetic field sweep range was set to 2800–4000 G, with a 25 dB attenuation, a modulation amplitude of 1.0 G, and a modulation frequency of 100 kHz.

Electrochemical Measurements

Galvanostatic charge–discharge profiles were obtained by assembling 2032-type coin cells consisting of an α-MnO_2 electrode, a glass fiber separator, and a Zn metal foil (250 μm, 99.98%, Alfa Aesar). The electrodes were fabricated by mixing α-MnO_2 active material, carbon black (Super P), and polyvinylidene fluoride (PVdF) in N-methyl-2-pyrrolidone (NMP) at a weight ratio of 6:2:2. The resulting slurry was cast onto a current collector (SUS 316 L foil, 20 μm thick) using the doctor blade method and dried at room temperature overnight. Electrochemical performance was evaluated using 40 μL of electrolyte: either 2 M $ZnSO_4$ or a mixed solution of 1 M $ZnSO_4 + 0.5$ M $Al_2(SO_4)_3$.

The GITT was performed using 10-minute current pulses at a current density of 0.3C (92.5 mA g^{-1}), followed by 5-hour rest periods to measure the QOCV within a voltage range of 0.9–1.9 V (vs. Zn/Zn^{2+}). For dQ/dV analysis, tests were conducted using two voltage windows: 1.4–1.9 V and 0.9–1.9 V (vs. Zn/Zn^{2+}). A custom H-cell setup was employed to record galvanostatic charge–discharge profiles in different electrolytes. A three-electrode configuration was used, with the Zn foil counter electrode placed in a compartment filled with 2 M $ZnSO_4$, and the Ag/AgCl reference electrode and α-MnO_2 working electrode placed in the compartment containing 1 M $ZnSO_4 + 0.5$ M $Al_2(SO_4)_3$. A Nafion-117 membrane, presoaked overnight in 2 M $ZnSO_4$, was used to separate the two compartments. This cell operated at a current density of 0.3C (92.5 mA g^{-1}), within a voltage range of −0.1–1.1 V (vs. Ag/AgCl) (corresponding to 0.9–2.1 V vs. Zn/Zn^{2+}). A Swagelok Union Tee cell was used for operando pH measurements and for recording galvanostatic charge–discharge profiles with pH variations in the electrolyte. These tests were conducted at a current density of 0.3C within a voltage range of −0.1–1.2 V (vs. Ag/AgCl). For operando pH monitoring, a pH electrode was connected to a ThermoFisher Orion Star A211 pH meter, positioned between the α-MnO_2 and Zn electrodes with 3 mL of the following electrolytes: 2 M $ZnSO_4 + 0.3$ M $MnSO_4$ and 1 M $ZnSO_4 + 0.5$ M $Al_2(SO_4)_3 + 0.2$ M $MnSO_4$. To evaluate the effect of electrolyte pH on charge–discharge behavior, α-MnO_2, Zn metal, and Ag/AgCl were used as the working, counter, and reference electrodes, respectively. The pH of 1 M $ZnSO_4 + 0.2$ M $MnSO_4$ electrolyte was adjusted to values of 1, 2, 3, and 4 by adding H_2SO_4 (95%, Daejung). The pH of the 2 M $ZnSO_4 + 0.2$ M $MnSO_4$ electrolyte was adjusted to 1 using two different acids: H_2SO_4 and HCl (35%–37%, Daejung). Similarly, the pH of the 1 M $ZnSO_4$ and 0.5 M $Al_2(SO_4)_3 + 0.2$ M $MnSO_4$ electrolyte was adjusted to 1 using H_2SO_4. Galvanostatic cycling was conducted at 0.3C using a three-electrode configuration, with α-MnO_2 as the working electrode, Zn metal as the counter electrode, and Ag/AgCl as the reference electrode. The cells were operated in a voltage range of −0.1–1.2 V (vs. Ag/AgCl). All galvanostatic charge–discharge experiments were carried out at 30 °C using a battery cycler system (WBCS3000, WonATech).

Acknowledgements

D.H.J. and E.J.J. contributed equally to this work. This work was supported by National Research Foundation of Korea (NRF) grant funded by the Korea government (MSIT) (RS-2024-00407015 and RS-2023-00261543) and by the Technology Innovation Program (20024818, Development of High-Strength Corrosion Resistant Lightweight Current Collector Material Technology for Sulfide-Based All-Solid-State Batteries) funded by the Ministry of Trade, Industry & Energy (MOTIE, Korea).

Conflict of Interest

The authors declare no conflict of interest.

Data Availability Statement

The data that support the findings of this study are available from the corresponding author upon reasonable request.

Keywords: aluminum sulfates · aqueous batteries · cell potential · manganese oxide cathodes · reaction mechanism

[1] B. Dunn, H. Kamath, J.-M. Tarascon, *Science* **2011**, *334*, 928.
[2] Y. Cao, M. Li, J. Lu, J. Liu, K. Amine, *Nat. Nanotechnol.* **2019**, *14*, 200.
[3] Y. Liu, Y. Zhu, Y. Cui, *Nat. Energy* **2019**, *4*, 540.
[4] J. Byun, C. R. Lee, W. Kim, M. A. Lee, H. Y. Jang, C. Hwang, J. H. Song, J.-S. Yu, S. Back, K. J. Kim, H.-S. Kim, *Adv. Funct. Mater.* **2024**, *34*, 2401620.
[5] Y. E. Durmus, H. Zhang, F. Baakes, G. Desmaizieres, H. Hayun, L. Yang, M. Kolek, V. Küpers, J. Janek, D. Mandler, S. Passerini, Y. Ein-Eli, *Adv. Energy Mater.* **2020**, *10*, 2000089.
[6] C. Qi, H. Wang, M. Li, C. Li, Y. Li, C. Shi, N. Wei, Y. Wang, H. Zhang, *Batteries*, **2025**, 11.

© 2025 Wiley-VCH GmbH

[7] X. Feng, M. Ouyang, X. Liu, L. Lu, Y. Xia, X. He, *Energy Storage Mater.* **2018**, *10*, 246.
[8] C. Zhang, S. Chou, Z. Guo, S.-X. Dou, *Adv. Funct. Mater.* **2024**, *34*, 2308001.
[9] D. Chao, W. Zhou, F. Xie, C. Ye, H. Li, M. Jaroniec, S.-Z. Qiao, *Sci. Adv.* **2020**, *6*, eaba4098.
[10] Y. Shang, D. Kundu, *Batteries & Supercaps* **2022**, *5*, e202100394.
[11] L. Kang, M. Cui, Z. Zhang, F. Jiang, *Batteries & Supercaps* **2020**, *3*, 966.
[12] X. Ji, L. F. Nazar, *Nat. Sustain* **2024**, *7*, 98.
[13] S. K. Mohanty, Y. Ok, E. S. Kim, Y. Park, J. H. Ryu, J. Mun, J. Lee, K. Hyun, M. K. Srinivasa, H. Jeong, S. C. Reddy, H. D. Yoo, *Batteries & Supercaps* **2024**, *7*, e202400338.
[14] V.-C. Ho, H. Lim, M. J. Kim, J. Mun, *Chem. Asian J.* **2022**, *17*, e202200289.
[15] V.-C. Ho, H. Yen Nguyen Thi, T. Huong Pham, H.-G. Jung, J. Ho Kim, J. F. Kim, J. Mun, *Chem. Eng. J.* **2024**, *496*, 153845.
[16] L. Du, X. Hou, X. Yang, V. Siozios, B. Yan, X. Ju, E. Paillard, M. Winter, T. Placke, J. Li, *Batteries & Supercaps* **2022**, *5*, e202100376.
[17] Z. Liu, Z. Guo, L. Fan, C. Zhao, A. Chen, M. Wang, M. Li, X. Lu, J. Zhang, Y. Zhang, N. Zhang, *Adv.Mater.* **2024**, *36*, 2305988.
[18] T. Wu, C. Hu, Q. Zhang, Z. Yang, G. Jin, Y. Li, Y. Tang, H. Li, H. Wang, *Adv. Funct. Mater.* **2024**, *34*, 2315716.
[19] F. Wang, O. Borodin, T. Gao, X. Fan, W. Sun, F. Han, A. Faraone, J. A. Dura, K. Xu, C. Wang, *Nat. Mater.* **2018**, *17*, 543.
[20] J. Huang, Z. Guo, Y. Ma, D. Bin, Y. Wang, Y. Xia, *Small Methods* **2019**, *3*, 1800272.
[21] S. H. Gong, H. J. Lim, J. H. Lee, Y. Yoo, S. Yu, H.-D. Lim, H. W. Jung, J. S. Ko, I. S. Kim, H.-S. Kim, *Appl. Surf. Sci.* **2023**, *611*, 155633.
[22] H.-g. Jo, E. Lee, S. Han, J. Lim, M. Jeong, J. Hwang, H.-D. Lim, H.-S. Kim, H. C. Ham, S. H. Oh, *Energy Storage Mater.* **2023**, *61*, 102881.
[23] J. Jang, W.-G. Lim, C. Jo, *Batteries & Supercaps* **2024**, *7*, e202400365.
[24] Z.-C. Zhang, Y.-B. Mu, L.-J. Xiao, X.-Y. Wei, M.-S. Han, C. Yang, L.-M. Zang, L. Zeng, J.-H. Qiu, *cMat* **2025**, *2*, e70000.
[25] D. Gupta, S. Liu, R. Zhang, Z. Guo, *Adv. Energy Mater.* **2025**, *15*, 2500171.
[26] D. Wang, L. Wang, G. Liang, H. Li, Z. Liu, Z. Tang, J. Liang, C. Zhi, *ACS Nano* **2019**, *13*, 10643.
[27] Y. Chen, J. Li, S. Zhang, J. Cui, M. Shao, *Adv. Mater. Interfaces* **2020**, *7*, 2000510.
[28] A. Hashem Abdelmohsen, S. A. El-khodary, N. Ismail, Z. Song, J. Lian, *Chem. Eur. J.* **2025**, *31*, e202403425.
[29] Z. Zhou, S. Xie, H. Cai, A. N. Colli, W. Monnens, Q. Zhang, W. Guo, W. Zhang, N. Han, H. Pan, X. Zhang, H. Pan, Z. Xue, X. Zhang, Y. Yao, J. Zhang, J. Fransaer, *Sci. Adv.* **2024**, *10*, eado7826.
[30] Z. Shao, L. Lin, W. Zhuang, S. Liu, P. Yang, K. Zhu, C. Li, G. Guo, W. Wang, Q. Zhang, Y. Yao, *Adv.Mater.* **2024**, *36*, 2406093.
[31] C. Li, W. Wang, J. Luo, W. Zhuang, J. Zhou, S. Liu, L. Lin, W. Gong, G. Hong, Z. Shao, J. Du, Q. Zhang, Y. Yao, *Adv.Mater.* **2024**, *36*, 2313772.
[32] H. Moon, K.-H. Ha, Y. Park, J. Lee, M.-S. Kwon, J. Lim, M.-H. Lee, D.-H. Kim, J. H. Choi, J.-H. Choi, K. T. Lee, *Adv. Sci.* **2021**, *8*, 2003714.
[33] Y. Ren, H. Li, Y. Rao, H. Zhou, S. Guo, *Energy Environ. Sci.* **2024**, *17*, 425.
[34] G. Liang, F. Mo, H. Li, Z. Tang, Z. Liu, D. Wang, Q. Yang, L. Ma, C. Zhi, *Adv. Energy Mater.* **2019**, *9*, 1901838.
[35] S. Wang, Z. Sang, X. Zhao, J. Guo, H. Chen, D. a. Yang, *Batteries & Supercaps* **2022**, *5*, e202100313.
[36] J. Shin, J. K. Seo, R. Yaylian, A. Huang, Y. S. Meng, *Int.Mater.Rev.* **2020**, *65*, 356.
[37] S. Gao, B. Li, H. Tan, F. Xia, O. Dahunsi, W. Xu, Y. Liu, R. Wang, Y. Cheng, *Adv.Mater.* **2022**, *34*, 2201510.
[38] Z. Shen, Y. Liu, L. Luo, J. Pu, Y. Ji, J. Xie, L. Li, C. Li, Y. Yao, G. Hong, *Small* **2022**, *18*, 2204683.
[39] L. Meng, Y. Zhu, Y. Lu, T. Liang, L. Zhou, J. Fan, Y.-C. Kuo, P. Guan, T. Wan, L. Hu, D. Chu, *ChemElectroChem* **2024**, *11*, e202300495.
[40] Z. Zheng, G. Yang, J. Yao, J. Li, J. Zheng, Z. Wu, Y. Gan, C. Wang, L. Lv, H. Wan, C. Chen, H. Wang, L. Tao, J. Zhang, H. Wang, *Appl. Surf. Sci.* **2022**, *592*, 153335.
[41] X. Xu, Y. Chen, W. Li, R. Yin, D. Zheng, X. Niu, X. Dai, W. Shi, W. Liu, F. Wu, M. Wu, S. Lu, X. Cao, *Small* **2023**, *19*, 2207517.
[42] J. Heo, S. Chong, S. Kim, R. Kim, K. Shin, J. Kim, H.-T. Kim, *Batteries & Supercaps* **2021**, *4*, 1881.
[43] B. G. Kim, S. W. Park, H. J. Choi, J.-W. Park, H. Lee, J.-H. Choi, *Small Methods* **2022**, *6*, 2101060.
[44] X. Gao, H. Wu, W. Li, Y. Tian, Y. Zhang, H. Wu, L. Yang, G. Zou, H. Hou, X. Ji, *Small* **2020**, *16*, 1905842.
[45] A. Konarov, N. Voronina, J. H. Jo, Z. Bakenov, Y.-K. Sun, S.-T. Myung, *ACS Energy Lett.* **2018**, *3*, 2620.
[46] X. Zhou, K. Ma, Q. Zhang, G. Yang, C. Wang, *Nano Res.* **2022**, *15*, 8039.
[47] N. Li, G. Li, C. Li, H. Yang, G. Qin, X. Sun, F. Li, H.-M. Cheng, *ACS Appl. Mater. Interfaces* **2020**, *12*, 13790.
[48] A. Ejigu, L. W. Le Fevre, A. Elgendy, B. F. Spencer, C. Bawn, R. A. W. Dryfe, *ACS ACS Appl. Mater. Interfaces* **2022**, *14*, 25232.
[49] C. Chen, M. Shi, Y. Zhao, C. Yang, L. Zhao, C. Yan, *Chem. Eng. J.* **2021**, 422.
[50] X. Chang, J. Chacón-Borrero, J. Shang, K. Xiao, G. Montaña-Mora, K. V. Mejia-Centeno, X. Lu, A. Yu, J. Yu, X. Zhou, S. Tunmee, P. Kidkhunthod, C. Cui, J. Li, Y. Tang, P. R. Martínez-Alanis, J. Arbiol, A. Cabot, *Adv. Energy Mater.* **2024**, *14*, 2402584.
[51] V. Balland, M. Mateos, A. Singh, K. D. Harris, C. Laberty-Robert, B. Limoges, *Small* **2021**, *17*, 2101515.
[52] Z. Qin, Y. Song, D. Yang, M.-Y. Zhang, H.-Y. Shi, C. Li, X. Sun, X.-X. Liu, *ACS Appl. Mater. Interfaces* **2022**, *14*, 10526.
[53] Y. Li, Y. Li, Q. Liu, Y. Liu, T. Wang, M. Cui, Y. Ding, H. Li, G. Yu, *Angew. Chem. Int. Ed.* **2024**, *63*, e202318444.
[54] S. Liang, F. Teng, G. Bulgan, R. Zong, Y. Zhu, *J. Phys. Chem. C* **2008**, *112*, 5307.
[55] M. Musil, B. Choi, A. Tsutsumi, *J. Electrochem. Soc.* **2015**, *162*, A2058.
[56] S. J. Kim, D. Wu, N. Sadique, C. D. Quilty, L. Wu, A. C. Marschilok, K. J. Takeuchi, E. S. Takeuchi, Y. Zhu, *Small* **2020**, *16*, 2005406.
[57] L. Godeffroy, I. Aguilar, J. Médard, D. Larcher, J.-M. Tarascon, F. Kanoufi, *Adv. Energy Mater.* **2022**, *12*, 2200722.
[58] K.-H. Ha, H. Moon, E. J. Joo, D. H. Jo, K. T. Lee, *Energy Storage Mater.* **2024**, *65*, 103150.
[59] F. Giacobello, V. Mollica-Nardo, C. Foti, R. C. Ponterio, F. Saija, S. Trusso, J. Sponer, G. Cassone, O. Giuffrè, *Liquids* **2022**, *2*, 26.
[60] F. L. Theiss, G. A. Ayoko, R. L. Frost, *Appl. Surf. Sci.* **2016**, *383*, 200.
[61] C. Wanner, R. Pöthig, S. Carrero, A. Fernandez-Martinez, C. Jäger, G. Furrer, *Geochim. Cosmochim. Acta* **2018**, *238*, 252.
[62] T. Clayton, *Mineral. Mag.* **1980**, *43*, 931.
[63] R. A. B. John W. Anthony, Kenneth W. Bladh, Monte C. Nichols, (Eds: *Handbook Of Mineralogy*, Mineralogical Society of America, Chantilly, VA 20151-1110, USA **2003**.
[64] P. Patnaik, *Dean's Analytical Chemistry Handbook*, 2nd Edition, McGraw-Hill Education, New York **2004**.

Manuscript received: March 28, 2025
Revised manuscript received: May 28, 2025
Version of record online:

© 2025 Wiley-VCH GmbH

25666223, 0, Downloaded from https://chemistry-europe.onlinelibrary.wiley.com/doi/10.1002/batt.202500238 by University of Ulsan, Wiley Online Library on [11/11/2025]. See the Terms and Conditions (https://onlinelibrary.wiley.com/terms-and-conditions) on Wiley Online Library for rules of use; OA articles are governed by the applicable Creative Commons License